RSC Mechanochemistry

ROYAL SOCIETY OF CHEMISTRY

PAPER

View Article Online
View Journal | View Issue

Cite this: *RSC Mechanochem.*, 2025, **2**, 443

Green mechanochemical fabrication of graphite-lanthanide oxide nanocomposites†

Diego A. Acevedo-Guzmán, *[ab] Brian Monroy-Torres, [b] Petra Rudolf, [a] Vladimir A. Basiuk [c] and Elena V. Basiuk *[b]

In this study, we explored mechanochemistry as a facile and environmentally friendly approach for the synthesis of graphite-lanthanide oxide nanocomposites. We determined the optimal conditions, namely a milling time of 48 h and milling ball size of 10 mm diameter, for which processing mixtures of graphite and lanthanide oxide in a planetary ball mill resulted in exfoliated graphene nanosheets functionalised with lanthanide oxide particles. The prepared nanocomposites were investigated by a suite of analytical techniques; X-ray photoelectron spectroscopy proved that mechanochemical processing in the presence of lanthanide oxides functionalises the graphene surface. Raman spectroscopy and X-ray diffraction results evidenced that the mechanochemical treatment exfoliates graphite and reduces the size of graphite crystallites. Scanning electron microscopy and scanning transmission electron microscopy confirmed the formation of lanthanide oxide nanoparticles and their uniform distribution on the graphene surface and thermogravimetric analysis gave evidence that the graphite-lanthanide oxide nanocomposites are less thermally stable than pristine graphite. The toxicity of the graphite-lanthanide oxide nanocomposites was also studied; we found that COS-7 monkey kidney cell growth was not inhibited for more than 5% in most of the studies.

Received 31st July 2024
Accepted 27th January 2025

DOI: 10.1039/d4mr00085d

rsc.li/RSCMechanochem

Introduction

The development of more sustainable and environmentally friendly synthetic methods for the functionalisation of graphene nanomaterials (GNMs) remains a persistent challenge. Currently, many physicochemical methodologies for the chemical modification of GNMs involve multi-step time-consuming processes and the use of environmentally harmful chemicals. Although many scalable approaches to graphene nanosheet (GN) production have been proposed,[1] several of them still rely on harmful solvents such as *N*,*N*-dimethylformamide, *N*-methyl-2-pyrrolidone[2] and strong acids,[3] generating toxic waste. More sustainable processes like the exfoliation of graphite in water[4–7] often necessitate additives like pyrene derivatives,[8,9] surfactants,[10] or supercritical CO_2.[11]

A prevalent route for the functionalisation of GNs starts with the oxidation of graphite to obtain graphene oxide (GO), where each single-atom carbon layer bears reactive oxygen-containing functional groups: hydroxyl and epoxy groups mainly located in the planes and mostly carbonyl and carboxyl groups[12] at the edges. The precise properties of GO depend on the degree of oxidation[13,14] and the oxidation method. Widely famous methods for the synthesis of GO, developed by Brodie,[15] Staudenmaier,[16] Hofmann,[17] and Hummers[18] and their modifications, generate corrosive and toxic waste, harmful to the environment and living organisms. Furthermore, the strong oxidising agents introduce several types of defects to the graphene nanosheets, and the subsequent reduction of GO often involves environmentally problematic agents such as hydrazine.[19] Consequently, it is imperative to develop efficient and environmentally friendly synthetic methodologies, which avoid the oxidation step with acids.

In recent years, ball milling has gained prominence in various areas of chemistry and materials science,[20,21] proving effective in nanoparticle synthesis[22,23] and graphite exfoliation[24,25] – a field known as mechanochemistry. Mechanochemistry, a sustainable and green technology, enables the functionalisation of carbon nanostructures[26–28] without the use of toxic and hazardous chemicals. Its advantages over solution-based methodologies include higher yields, elimination of the use of organic solvents, cost-effective mass production of graphene,[29] scalability, reduced waste generation, improved energy and atom economy.[30]

Several research groups have successfully applied mechanochemical methods to exfoliate and oxidise graphite[31–37] utilising a planetary mill and shown that the oxygen content increases with milling time.[33] The moving balls transfer energy

[a]*Zernike Institute for Advanced Materials, University of Groningen, Nijenborgh 4, 9747 AG Groningen, The Netherlands. E-mail: diegoaag94@gmail.com*

[b]*Instituto de Ciencias Aplicadas y Tecnología, Universidad Nacional Autónoma de México, Circuito Exterior C.U., 04510 Cd. Mexico, Mexico*

[c]*Instituto de Ciencias Nucleares, Universidad Nacional Autónoma de México, Circuito Exterior C.U., 04510 Cd. Mexico, Mexico*

† Electronic supplementary information (ESI) available. See DOI: https://doi.org/10.1039/d4mr00085d

to the milled graphite powder, breaking strong covalent bonds and producing reactive surfaces.[38] Thus, by combining exfoliation and chemical functionalisation, this approach becomes suitable for large-scale graphene nanocomposite production.

The last decade has witnessed the fabrication of graphene-lanthanide nanohybrids primarily for supercapacitors and dye adsorbents in water remediation,[39–46] fluorescent nanoprobes for tumour-targeted imaging,[47] detection of bacterial spores and cysteine,[48] or catalysts for high-performance hydrogen evolution and oxygen reduction.[49] However, only a few studies have explored sustainable synthetic routes using graphite and lanthanide oxides (LnO) as the main precursors. In our previous work[50] we explored mechanochemistry as a facile one-step strategy for the synthesis of graphite-lanthanide oxide nanocomposites. In that first attempt, the milling conditions were not optimal, leading to excessive graphite fragmentation and the production of amorphous carbon. In addition, the size of the LnO particles and their distribution on the graphite flakes was not uniform.[50] Here we present the results of the optimisation of the processing conditions, where excessive graphite fragmentation and amorphisation are avoided and the distribution of lanthanide oxide nanoparticles is much improved. The success of the optimised processing with a milling ball size of 10 mm diameter instead of the 20 mm used previously and an increased milling time of 48 hours (before only 8 h were used), demonstrates mechanochemistry as a robust and environmentally friendly strategy for the efficient fabrication of low-defect graphite-lanthanide oxide nanocomposites.

Experimental

Materials

Lanthanide (Ln) oxides La_2O_3, Eu_2O_3, Gd_2O_3, and Tb_4O_7 (all having 99.9% purity), as well as graphite powder (particle size of <20 μm) were purchased from Sigma-Aldrich and used as received.

Mechanochemical functionalisation

The synthesis of graphite-lanthanide oxide (graphite-Ln) nanocomposites involved the use of mixtures containing 10 wt% lanthanide oxide. The specific details for each sample are outlined below:

For the samples graphite-La, graphite-Eu, graphite-Gd, and graphite-Tb, 3.6 g of graphite powder and 0.4 g of Ln oxide were combined. For the sample graphite-Eu-Gd, 3.6 g of graphite powder, 0.2 g of Eu_2O_3, and 0.2 g of Gd_2O_3 were mixed. Each mixture was placed in a 50 mL tungsten carbide (WC) reactor together with 20 WC balls of 10 mm diameter. The balls : mixture ratio was 22 : 1 w/w. After sealing the reactor, each sample was subjected to high-energy ball-milling for 48 h at 400 rpm using a Planetary Ball-Mill XQM-0.4A from Tencan. The process is illustrated in Fig. 1.

Characterisation

The X-ray photoelectron spectroscopy (XPS) measurements were carried out on a Surface Science Instruments SSX-100 ESCA instrument with a monochromatic Al Kα X-ray source ($h\nu$ = 1486.4 eV); the pressure in the chamber was maintained at 1×10^{-9} mbar during data acquisition and the electron take-off angle with respect to the surface normal was 37°. The XPS data were acquired by using a spot size of 1000 μm in diameter and the energy resolution was 1.3 eV; XPS spectra were analysed using the least-squares curve-fitting program Winspec (developed at the LISE laboratory of the University of Namur, Belgium). Powder samples were dispersed in isopropanol, sonicated for 5 min, and drop-casted on a thin gold film, grown on mica.[51] Peak profiles were taken as a convolution of Gaussian and Lorentzian functions and a Shirley background was used; binding energies (B.E.s) were referenced to the Au $4f_{7/2}$ photoemission peak centred at 84.0 eV (ref. 52) and are accurate to ± 0.1 eV when deduced from the fitting procedure. The uncertainty in the peak intensity determination is within 2% for all core levels reported. All measurements were carried out on freshly prepared samples; three spots were measured for each sample to check for homogeneity.

Raman spectra were acquired using a Witec alpha300R confocal Raman microscope (WITec GmbH, Ulm, Germany) equipped with a Nd:YVO4 laser providing 532 nm wavelength light. The incident laser beam, with a power of 2.85 μW, was focused on the sample using a 100× objective (Zeiss, 0.9 NA). The spectra in the range of 500–4000 cm^{-1} were collected in 10 randomly chosen points of each sample. Each spectrum was the average of 60 scans collected at 0.5 cm^{-1} resolution.

Powder X-ray diffraction (XRD) patterns were collected on a D8 Advance Bruker diffractometer in Bragg–Brentano

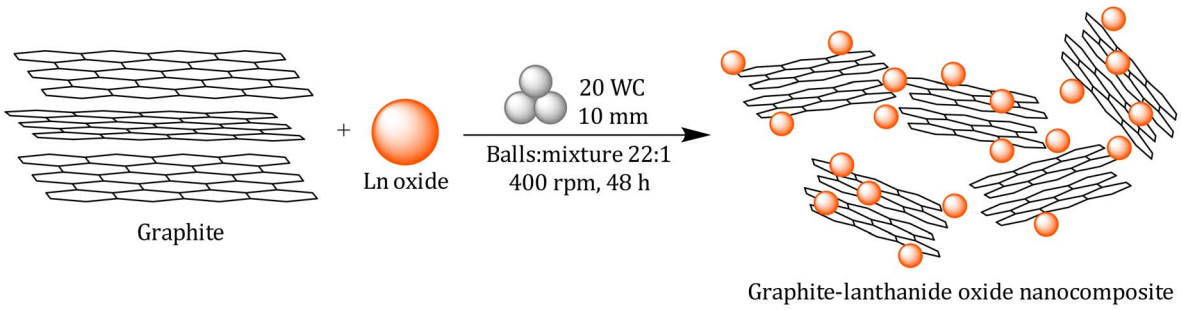

Fig. 1 Mechanochemical preparation of graphite-lanthanide oxide nanocomposites.

geometry with a monochromatic Cu Kα X-ray source (wavelength of 1.5418 Å) and a Lynxeye detector. Powder samples were placed on a zero-background holder and their patterns were recorded in a 2θ range from 5 to 70°, in steps of 0.02° and with a counting time of 0.75 s per step.

Scanning electron microscopy (SEM) and scanning transmission electron microscopy (STEM) characterisation were performed using a FEI NovaNano NanoSEM 650 instrument with an acceleration voltage of 20 kV. The powder samples were mounted on carbon tape for the SEM measurements. For the STEM measurements, the samples were dispersed in isopropanol, sonicated for 2 min, and drop-casted using standard Cu grids with holey carbon films.

Thermogravimetric (TGA) and differential thermal analysis (DTA) were performed in air on an STD 2960 Simultaneous DSC-TGA analyser from TA Instruments. Samples of ~5 mg were used; the airflow was 100 mL min^{-1} and a heating ramp of 10 °C min^{-1} up to 1000 °C was applied.

Cytotoxicity activity

The healthy monkey kidney cell line COS-7 was cultured in RPMI-1640 (Gibco®) supplemented with foetal bovine serum (10% v/v), nonessential amino acids (1% v/v), and penicillin-streptomycin solution (1% v/v) (Corning®). The cells were maintained at 37 °C in a humidified atmosphere with 5% CO_2. Cytotoxicity was tested by the sulforhodamine B (SRB) assay. Cells were seeded in a 96-well plate and incubated with fresh media or nanomaterial-water dispersions at 50 and 100 μg mL^{-1} concentration for 48 h, then cell monolayers were fixed directly to medium supernatant by adding cold trichloroacetic acid (50% wt/v) to each well. After incubation for 1 h at 4 °C, the plates were gently washed with water and dried at room temperature. To stain the cells, 100 μL of SRB (0.4% wt/v) were added to each well, left at room temperature for 30 min, and then washed with acetic acid (1% v/v) to remove the unbound dye. After drying at ambient conditions, the bound dye was solubilised by adding 100 μL tris base solution (10 mM) and shaking on an orbital shaker for 10 min. The absorbance was obtained at 515 nM in a microplate reader (SYNERGY HT, BioTek). Images were captured by an inverted microscope (DIAPHOT 300 Nikon®, Japan) with a digital camera (AmScope MD500) after 48 h treatment. The Growth inhibition (%) was calculated using the following equation:

$$\text{Growth inhibition (\%)} = 100 - [(\text{Abs. treatment}/\text{Abs. control}) \times 100]$$

Experiments were carried out in triplicate. Data are expressed as mean ± standard deviation. Statistical analysis was performed with GraphPad Prism 10, using a two-way ANOVA obtained significance with Tukey's multiple comparisons tests.

Results and discussion

Mechanochemical processing leads to the production of diverse carbon nanostructures, including multi-layered, few-layered, and single-layered graphene, as well as GO.[33,53] As sketched in Fig. 2, the milling process subjects graphite crystallites to impacting, compressive, shearing and collision forces. Compressive forces break the graphene sheets, reducing the particle size, while the shear forces induce exfoliation. To gain information on the type of functional groups present before and after mechanochemical processing of graphite alone and of the graphite-lanthanide oxide mixtures, XPS was employed.

The survey spectra of all milled samples and the detailed spectra of the Ln 3d photoemission lines are shown in Fig. S1–S7,† and it is confirmed that the samples are free of impurities like W from the milling balls employed. The C 1s core level spectra of pristine and ball milled graphite, along with the corresponding fits, are shown in Fig. 3. Table 1 provides the binding energy (B.E.) values of the various components deduced from the fits, and Table 2 summarises the relative intensities of the components. For pristine graphite, the presence of oxygen functionalities is evident even before the mechanochemical treatment. The observed components are attributed to C=C (at a B.E. of 284.5 eV), C–C/C–H (285.6 eV), C–OH/C–O–C (286.4 eV), C=O (287.8 eV), and O–C=O (289.3 eV), with C=C and C–C/C–H contributing the highest relative spectral intensity to the C 1s peak, as shown in Table 2. Considering the stoichiometry, in the pristine material the carbon and oxygen content was deduced to be 94.9 at% and 5.1 at%, respectively. Post-milling, the type of bonds detected remained the same, but their relative contribution to the total C 1s peak intensity changed. Specifically, the intensity of the component related to C=C bonds (associated with the sp^2 carbon atoms of the graphene lattice) decreased, while that due to C–C/C–H bonds increased, as expected if the size of the graphite flakes is smaller after the mechanochemical treatment.[54] Simultaneously, the oxygen content increased from 5.1 at% to 14.6 at% (see Table 2), accompanied by an increase in the contribution of C–OH/C–O–C and C=O bonds to the C 1s peak intensity. This confirms that milling in air creates epoxy, hydroxyl, and carbonyl groups on the graphene sheets, producing a material resembling reduced graphene oxide in the composition.[55] Since hydroxyl (C–OH) and epoxy (C–O–C) groups are known to be located mainly on the basal plane, while carbonyl (C=O) and carboxyl (COOH) groups usually decorate the edges of graphene,[56–59] we can conclude that both the basal plane and the edges of graphene sheets are functionalised simultaneously under our processing conditions. This contrasts with previous findings,[60–65] where mechanochemical functionalisation of graphene was reported to be highly edge-selective, both in the presence of additives like dry ice,[60–62] solid urea[63] or oxidants like $KMnO_4$ and $KHSO_4$ (ref. 64) and when milling in air as in this study.[65]

The C 1s spectra of all the five graphite-Ln nanocomposites (Fig. 4) exhibit the same components present in pristine and ball milled graphite, namely C=C, C–C/C–CH, C–OH/O–C–O, C=O, and O–C=O, but the addition of lanthanide oxides to the milling media seems to influence the efficiency of the mechanochemical processing, as we have seen in the past.[50] For all the graphite-Ln nanocomposites, the contribution of the C–OH/O–C–O component to the C 1s photoemission line is more important than for pristine graphite, implying the formation of

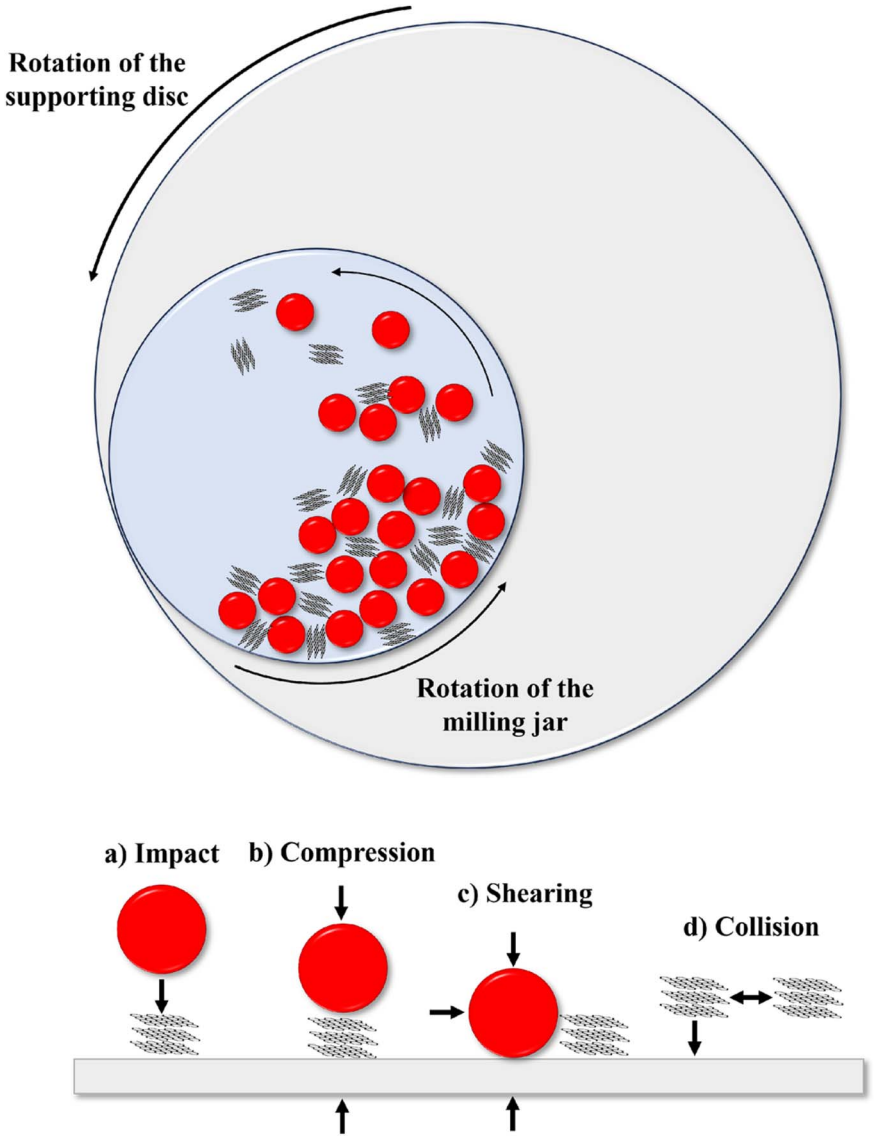

Fig. 2 Mechanism of graphite processing in a planetary mill (top) and forces to which the graphite flakes are subjected (bottom).

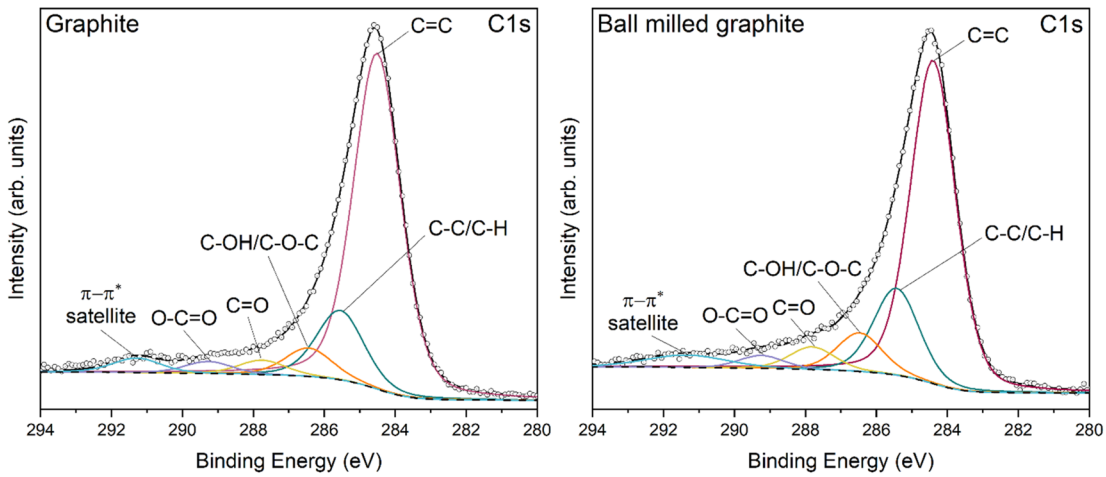

Fig. 3 Comparison of the C 1s core level spectra of pristine graphite and ball milled graphite and the corresponding fits.

Table 1 XPS binding energies of C 1s core level components of pristine graphite and ball milled graphite, as well as of the graphite-Ln nanocomposites

Sample	C=C [eV]	C–C/C–H [eV]	C–OH/C–O–C [eV]	C=O [eV]	O–C=O [eV]
Graphite	284.5	285.6	286.4	287.8	289.3
Ball milled graphite	284.4	285.4	286.5	287.8	289.2
Graphite-La	284.5	285.5	286.6	288.0	289.3
Graphite-Eu	284.5	285.6	286.7	288.0	289.4
Graphite-Gd	284.5	285.6	286.8	287.8	289.0
Graphite-Tb	284.5	285.5	286.5	287.9	289.3
Graphite-Eu-Gd	284.5	285.6	286.7	288.0	289.4

Table 2 Relative contributions of the various components to the total C 1s core level photoemission intensity and elemental composition of pristine and ball milled graphite, as well as of the graphite-Ln nanocomposites

	Percentage of the relative contribution to the C 1s XPS spectral intensity [%]					Composition [at%]		
Sample	C=C	C–C/C–H	C–OH/C–O–C	C=O	O–C=O	C	O	Ln
Graphite	70.6	14.6	6.0	3.0	2.5	94.9 ± 1.9	5.1 ± 0.1	—
Ball milled graphite	63.8	17.2	7.6	4.5	2.6	85.4 ± 1.7	14.6 ± 0.3	—
Graphite-La	64.6	17.3	7.0	3.3	2.6	82.2 ± 1.6	17.6 ± 0.4	0.2 ± 0.0
Graphite-Eu	64.1	21.4	7.3	2.6	2.4	87.2 ± 1.7	12.2 ± 0.2	0.6 ± 0.0
Graphite-Gd	61.6	19.7	7.8	2.0	2.6	83.4 ± 1.6	16.0 ± 0.3	0.6 ± 0.0
Graphite-Tb	67.5	14.9	7.1	3.2	1.9	82.4 ± 1.6	17.2 ± 0.3	0.3 ± 0.0
Graphite-Eu-Gd	61.0	18.6	7.0	3.9	2.5	85.3 ± 1.7	14.1 ± 0.3	0.3/0.3 ± 0.0

hydroxyl and epoxy groups during ball-milling. More importantly, the C–OH/O–C–O component shifts to higher binding energies: by 0.4 eV for graphite-Gd, and by 0.3 eV for graphite-Eu, and graphite-Eu-Gd. Moreover, the contribution of the C=O bonds to the C 1s photoemission signal, is higher for graphite-Eu-Gd, graphite-La, and graphite-Tb nanocomposites,

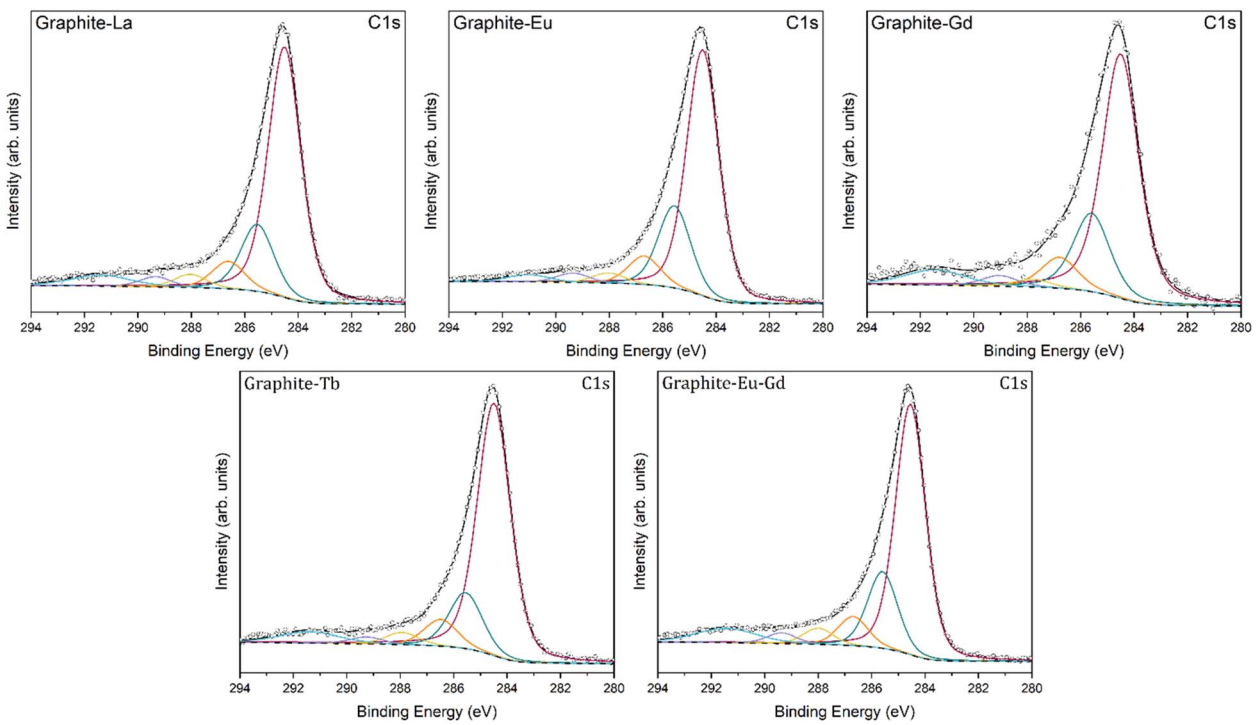

Fig. 4 Comparison of the C 1s core level spectra of graphite-Ln nanocomposites and the corresponding fits. The components are the same as in Fig. 3 – for details see text.

while for graphite-Eu and graphite-Gd it is lower compared to pristine graphite. Besides that, the C=O component shifts to lower binding energy by 0.2 eV for graphite-La, graphite-Eu, and graphite-Eu-Gd nanocomposites. These results suggest that lanthanide ions can be ionically/coordinatively anchored to the oxygen-containing functional groups on the graphene nanosheets. For all the graphite-Ln nanocomposites, the relative intensity of the O–C=O component and its binding energy remains practically unchanged with respect to pristine and ball milled graphite. In summary, these results show that the incorporation of lanthanide oxides in the milling media results in changes in the chemical functionalisation of graphene, and this effect is more pronounced in the presence of europium and gadolinium ions, in agreement with our previous work.[50]

Raman spectroscopy is a powerful non-destructive technique to characterise graphitic structures and carbon nanomaterials in general.[60–70] The Raman spectra of pristine graphite, ball milled graphite and graphite-Ln nanocomposites are shown in Fig. 5; the Raman shift for the D, G and 2D bands, as well as the calculated values of the I_D/I_G ratio and crystallite size (L_a), are summarised in Table 3. The Raman spectrum of pristine graphite is dominated by the G band and the 2D band. The G band appears as a strong symmetric sharp peak located at 1578 cm^{-1} and is attributed to first-order scattering of the E_{2g} phonon from the in-plane vibration of the sp^2 hybridised carbon lattice.[65–68] The 2D band at 2716 cm^{-1}, associated with the ordered stacked graphite structure along the *c*-axis, has an asymmetrical shape, characteristic of the multilayer nature of the pristine graphite sample.[69–74] Moreover, the D band associated with the vibrational mode A_{1g}, known as the breathing mode, and originating from a disruption in the hexagonal symmetry of the graphene backbone like structural defects, vacancies, crystal edges and sp^3 carbon domains,[70,71,73–75] appears as a low-intensity peak located at 1354 cm^{-1}. The ratio between the intensities of the D and the G band, I_D/I_G, is 0.07, which confirms that the sample consists of high-quality graphite with large grain sizes.[33,53,76,77] As expected, the I_D/I_G ratio deduced from the Raman spectrum of ball milled graphite is much higher, namely 0.62, indicating that the crystallite sizes have become smaller and that the mechanochemical treatment has created vacancies and defects as well as epoxy, hydroxyl, and carbonyl groups on the graphene sheets, as corroborated by the XPS results. This differs from what has been observed in our previous work as well as in other studies,[33,50,53,76] where the Raman spectra of graphite after the mechanochemical treatment looked like the typical GO spectrum with I_D/I_G ratios close to 1. This confirms that the optimised conditions for ball milling used here allow to functionalise the graphene surface without introducing a high amount of disorder in the lattice. Moreover, the shape of the G band is no longer symmetrical as for pristine graphite, but shows a shoulder around 1605 cm^{-1}, a Raman shift associated with the D′ band, demonstrating the presence of few-layered graphene.[31–34,63,70,78–80] This contrasts with the results of the mechanochemical preparation of graphite-phthalocyanine composites, where an effect of 'glueing' between graphite platelets and phthalocyanines was

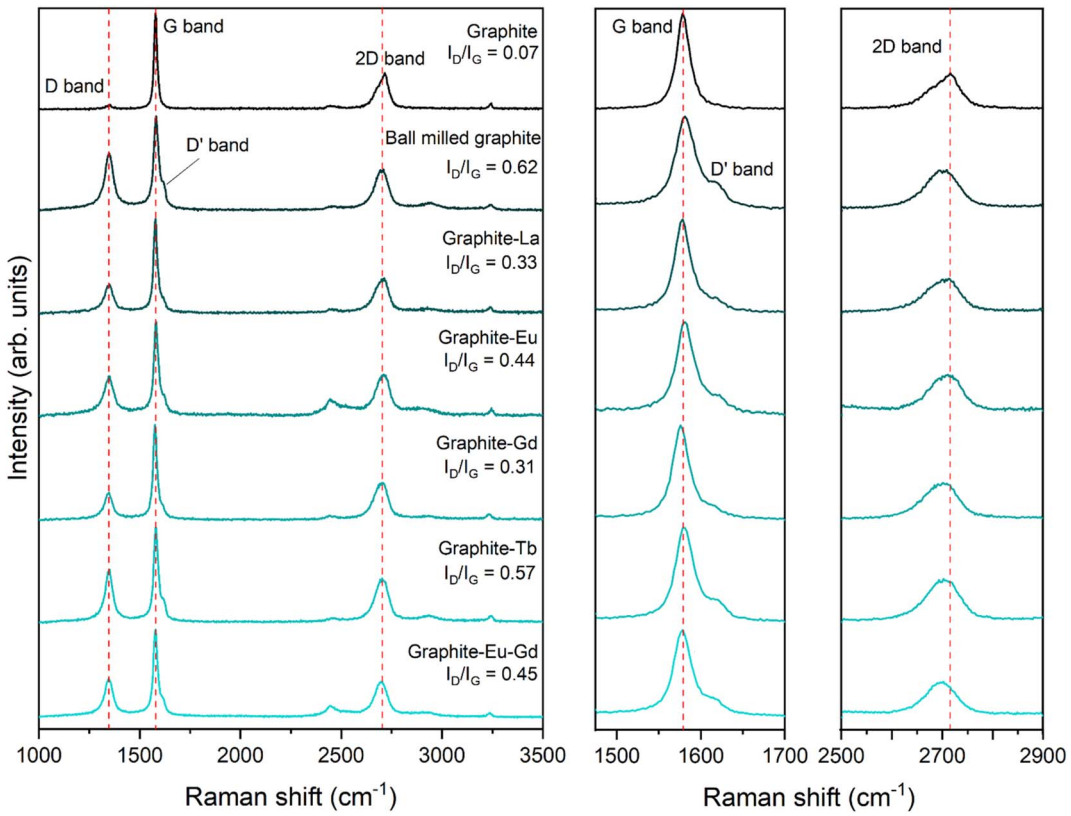

Fig. 5 Comparison of Raman spectra of pristine graphite, ball milled graphite, and graphite-Ln nanocomposites.

Table 3 Raman shift, I_D/I_G ratio and crystallite L_a size of graphite and ball milled graphite, as well as of the graphite-Ln nanocomposites

Sample	D band [cm^{-1}]	G band [cm^{-1}]	2D band [cm^{-1}]	I_D/I_G	L_a [nm]
Graphite	1354	1578	2716	0.07	291.5
Ball milled graphite	1349	1581	2709	0.62	32.9
Graphite-La	1349	1578	2707	0.33	61.8
Graphite-Eu	1352	1581	2709	0.44	46.4
Graphite-Gd	1349	1576	2702	0.31	65.8
Graphite-Tb	1351	1578	2702	0.57	35.8
Graphite-Eu-Gd	1343	1575	2702	0.45	45.3

Table 4 XRD values of (002) peak, FWHM, *d*-spacing and crystallite L_c size of graphite and BM graphite, as well as of the graphite-Ln nanocomposites

Sample	(002) Position [°]	(002) FWHM [°]	*d*-spacing [nm]	L_c [nm]
Graphite	26.5	0.3	0.34	32.3
Ball milled graphite	26.5	0.4	0.34	19.6
Graphite-La	26.5	0.3	0.34	24.0
Graphite-Eu	26.5	0.3	0.34	26.8
Graphite-Gd	26.5	0.3	0.34	27.1
Graphite-Tb	26.5	0.3	0.34	29.5
Graphite-Eu-Gd	26.5	0.3	0.34	28.5

observed under the same milling conditions.[81] One also notices that the 2D band downshifts to 2709 cm^{-1} and looks symmetrical, testifying to the fact that ball milled graphite keeps a proper Bernal stacking and further supporting the interpretation that graphite was partially exfoliated into few-layer graphene.[32–34,76,78,81–85] Taken together the Raman spectra prove that in comparison to our previous study, changing the milling time from 8 to 48 hours and the milling ball size from 20 mm to 10 mm diameter in order to reduce their impact energy, led to an improvement with respect to our previous results where the creation of few-layered graphene could not be confirmed (Table 4).[50]

Regarding the Raman spectra of the graphite-Ln nanocomposites, the observed changes are practically the same as those for ball milled graphite; the G band is asymmetrical due to the appearance of the D′ band, the 2D band shifts to lower Raman shift values, and the I_D/I_G ratio is higher than that for pristine graphite but lower than that of ball milled graphite. The I_D/I_G values were employed to calculate the in-plane sp^2 crystallite size (L_a) of graphite by following the equation given by Cançado *et al.*:[86]

$$L_a = (2.4 \times 10^{-10})(\lambda_{laser})^4/(I_D/I_G)$$

where λ is the wavelength of the laser source (nm). The graphite crystallite sizes deduced were as follows: pristine graphite 291.5 nm > graphite-Gd 65.8 nm > graphite-La 61.8 nm > graphite-Eu 46.4 nm > graphite-Eu-Gd 45.3 nm > graphite-Tb 35.8 nm > ball milled graphite 32.9 nm. These results indicate that the addition of lanthanide oxides to the milling media reduces the amount of disorder introduced to the graphene lattice without hindering the exfoliation of graphene nanosheets or their surface functionalisation with oxygen functional groups.

The X-ray diffraction (XRD) measurements were taken to track the changes in the crystalline nature of graphite and the lanthanide oxides (Fig. 6) produced by the mechanochemical treatment. The pristine graphite diffractogram shows two peaks located at 26.5° and 54.6°, corresponding to the (002) and (004) planes, respectively. The sharp and intense (002) peak is a clear indication of a highly ordered material with several graphene layers. Mechanochemically treated graphite maintained these two peaks, with the (002) peak showing no significant change in position or shape, suggesting that the milling process did not induce amorphisation even after 48 h of milling time. This contrasts with literature reports stating that milling times longer than 16 h produce a combination of crystalline and amorphous carbon.[33,53,76,87]

Interestingly, the introduction of lanthanide oxides in the milled mixture led to a drastic reduction in the intensity of the (002) peak in graphite-Ln nanocomposites (Fig. 7), suggesting a more efficient exfoliation of graphite layers facilitated by lanthanide oxides, as supported by the Raman spectroscopy results discussed above. This enhanced exfoliation can be attributed to a lubrication effect provided by lanthanide oxides, favouring shear forces over compressive forces during milling and promoting the slipping of graphene sheets. Despite the reduced intensity of the (002) peak, the position and sharpness remained unchanged, indicating that both graphite and lanthanide oxides retained their crystallinity. Furthermore, the characteristic peaks of lanthanide oxide hexagonal crystal structures were evident in graphite-Ln diffractograms, albeit with lower intensity compared to the graphite (002) peak due to the employed graphite : lanthanide oxide ratio. This observation underscores the preservation of lanthanide oxide crystallinity during the milling process. The graphite layer-to-layer *d*-spacing deduced from the XRD data did not reveal any significant differences between samples, which indicates that neither oxygen-containing functional groups nor the addition of lanthanide oxides affected the stacking pattern of graphene sheets. However, the apparent crystallite size along the *c*-axis of graphite decreased with the incorporation of lanthanide oxides, suggesting a role in reducing abrasive effects during mechanochemical treatment and producing smaller, low-defect crystallites. In detail, the coherently diffracting domains were slightly different in size for the different nanocomposites: graphite-Tb (29.5 nm) > graphite-Eu-Gd (28.5 nm) > graphite-Gd

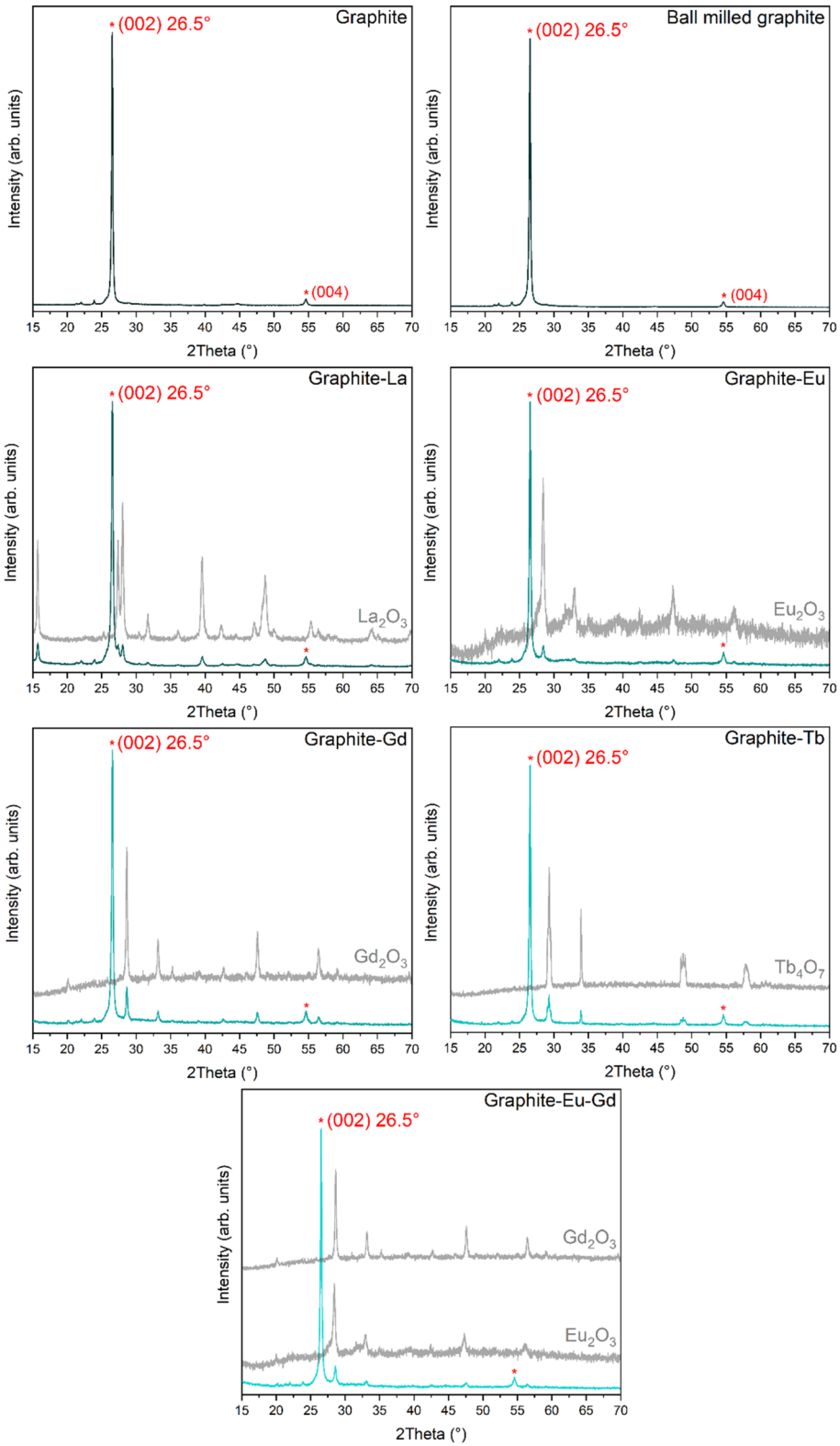

Fig. 6 XRD diffractograms of pristine graphite, ball milled graphite and graphite-Ln nanocomposites.

(27.1 nm) > graphite-Eu (26.8 nm) > graphite-La (24.0 nm), always smaller than that of pristine graphite (32.3 nm) but much larger than that of ball milled graphite (19.6 nm).

The effects of the mechanochemical treatment on the graphite morphology were explored by scanning electron microscopy (Fig. 8). The micrographs of pristine graphite show

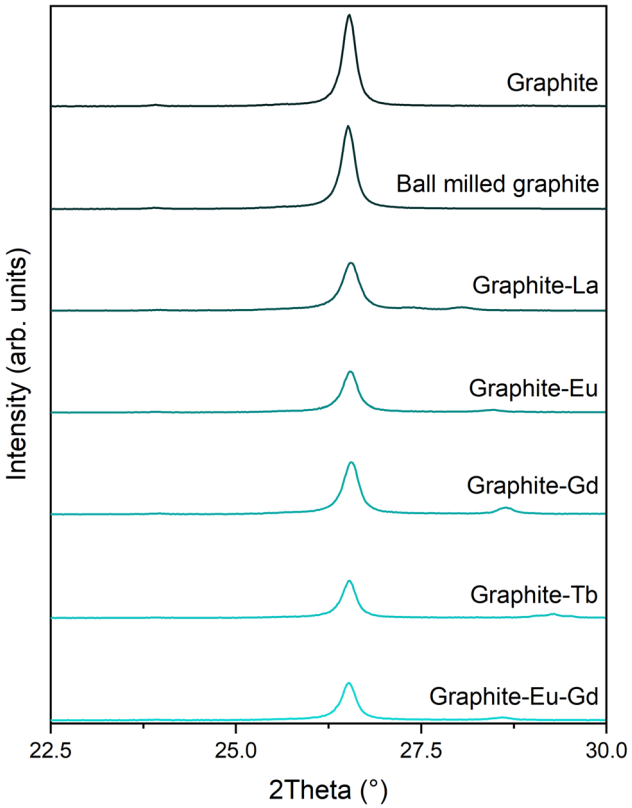

Fig. 7 Comparison of the (002) peak of pristine graphite, ball milled graphite and graphite-Ln nanocomposites.

thick flaky crystals with sharp edges, smooth surfaces and variable crystallite sizes ranging from 5 to 20 μm. After the mechanochemical treatment, the crystallite size decreased, and platelets had lateral dimensions ranging from 1 to 7 μm while preserving the stacked structure. These images confirm again that the optimised milling conditions represent a great improvement with respect to those of our previous study, where we found abundant amorphous debris after the mechanochemical treatment.[50]

Similar morphology changes were observed for the graphite-Ln nanocomposites (Fig. 9), here the lateral dimensions of the graphite flakes varied between 1 to 6 μm. The images generated by backscattered electrons (Fig. 9, SEM-BE), which allow to differentiate between light and heavy elements in a sample, demonstrated a uniform dispersion of micro- and nanosized lanthanide oxide particles throughout the graphite surface, pointing to an improved particle distribution compared to previous studies.[50]

More detailed information about the size of the lanthanide nanoparticles is provided by scanning transmission electron microscopy images (Fig. 9), acquired with the high-angle annular dark-field detector (STEM-HAADF). The micrographs show that most lanthanide oxide particles (marked with yellow dashed circles) have sizes of around 170–340 nm for graphite-La, 60–140 nm for graphite-Eu, 60–110 nm for graphite-Gd, 80–190 nm for graphite-Tb and 50–200 nm for graphite-Eu-Gd. In addition, a few smaller lanthanide oxide particles can be discerned. Eu_2O_3 and Gd_2O_3 particles are smaller than other lanthanide oxides employed, probably due to the higher interaction between the oxygen-containing groups on graphene and the lanthanide ions deduced from the XPS results. The stacked layers of graphene are also clearly seen, confirming the presence of few-layer graphene.

Thermal analysis vis TGA-DTA (Fig. 10) provided insights into the thermal stability of graphite and the influence of both mechanochemical treatment and the presence of lanthanide oxides. The thermogram of pristine graphite exhibited a single weight loss event starting around 560 °C and ending at 836 °C, associated with the total combustion of the graphitic carbon network, with the corresponding DTA peak centred at 794 °C.

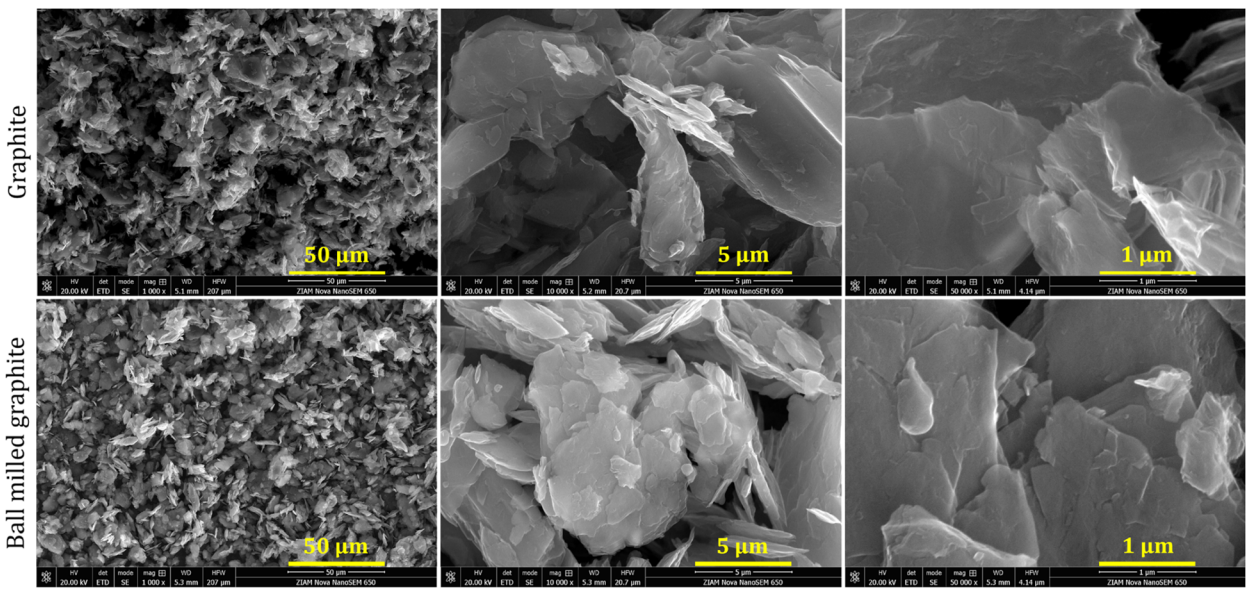

Fig. 8 SEM-SE micrographs of pristine graphite and ball milled graphite.

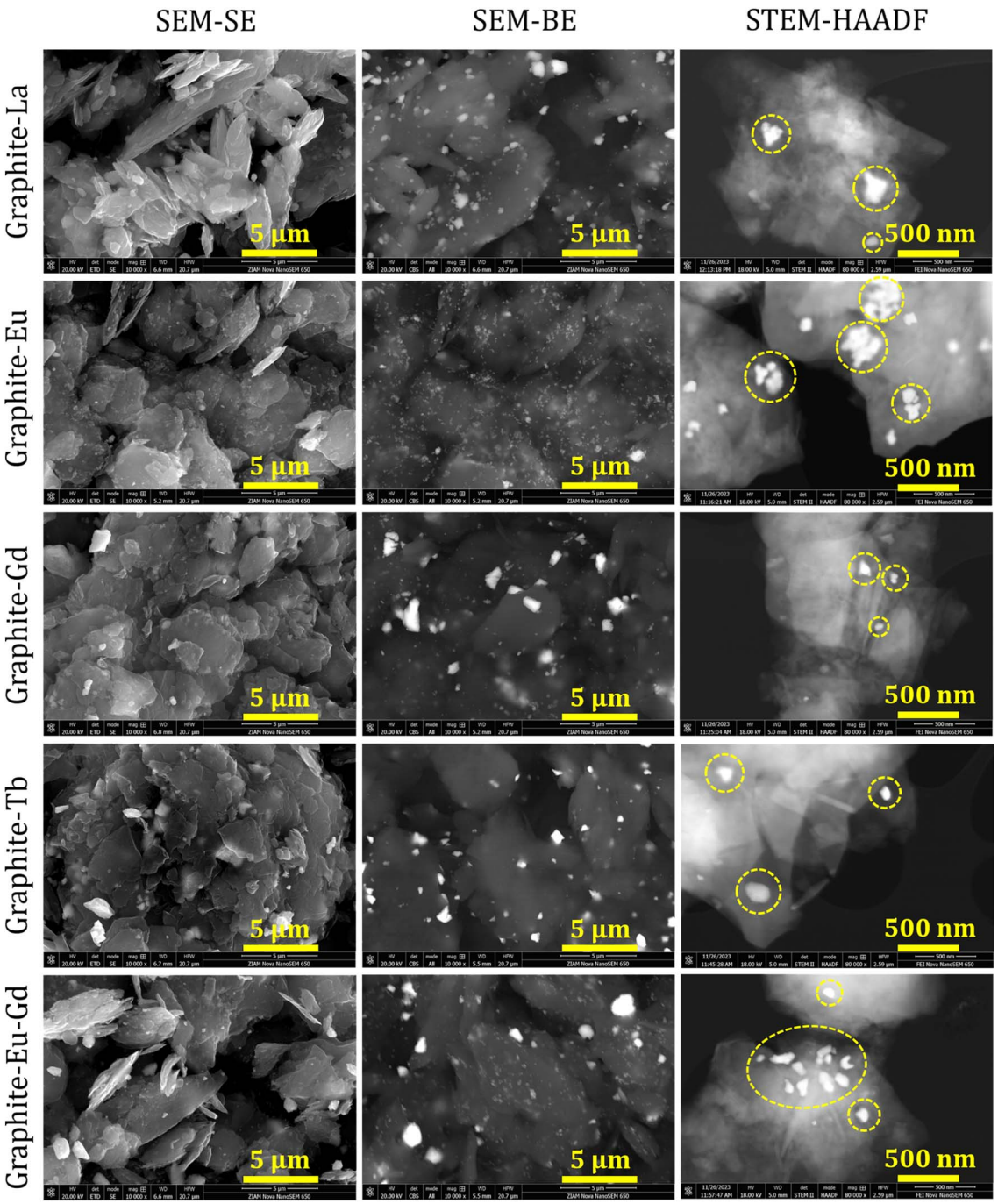

Fig. 9 Scanning electron microscopy SEM-SE (left column), SEM-BE (central column) and transmission electron microscopy micrographs STEM-HAADF (right column) of graphite-Ln nanocomposites (yellow circles show some of the nanoparticles). Note that since STEM-HAADF images were collected on Cu grids, the spot on the sample is different.

Mechanochemical processing reduced the thermal stability of graphite, as evidenced by the thermogram of ball milled graphite, which showed a lower onset of combustion at around 520 °C, with a DTA peak centred at 745 °C. This decrease in temperature can be explained by the introduction of new reactive sites, defects, and oxygen functionalities during milling, consistent with the findings from XPS, Raman, XRD and SEM discussed earlier.

The thermograms of the graphite-Ln nanocomposites revealed varying temperatures for the final combustion: 750 °C for graphite-La, 792 °C for graphite-Eu, 837 °C for graphite-Gd, 823 °C for graphite-Tb, and 811 °C for graphite-Eu-Gd. As for the material ball milled, the weight loss started before 550 °C for all the lanthanide-containing nanocomposites due to the presence of oxygen-containing functional groups.

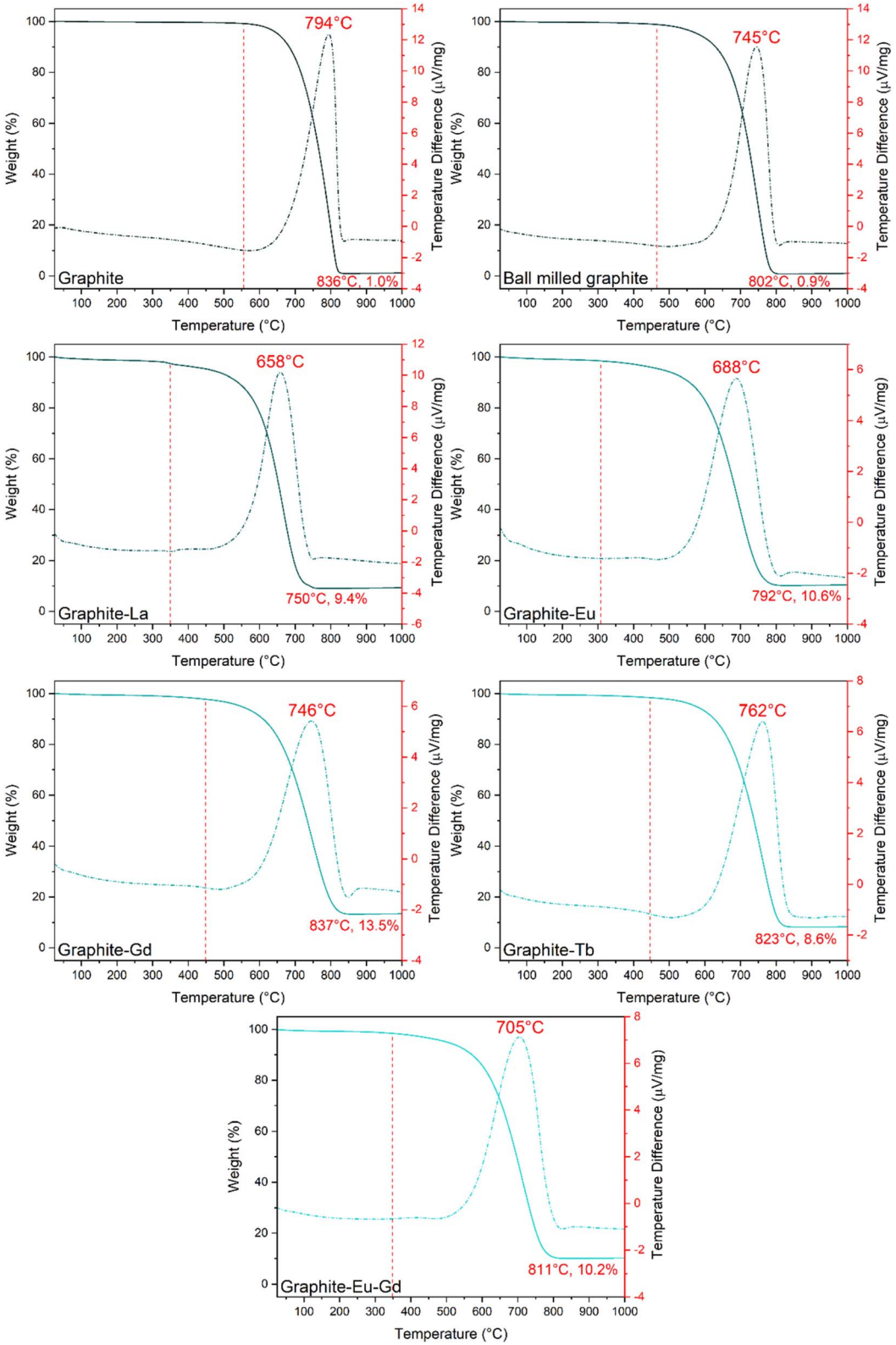

Fig. 10 Thermograms of graphite, ball milled graphite, and graphite-Ln nanocomposites.

Interestingly, the observed final combustion temperatures did not strictly correlate with the Raman I_D/I_G ratio. Only graphite-La and graphite-Eu show a considerable decrease in the final combustion temperature, of 750 °C and 792 °C, respectively, pointing to a possible catalytic effect of the La and Eu oxides. Graphite-Gd, graphite-Tb and graphite-Eu-Gd

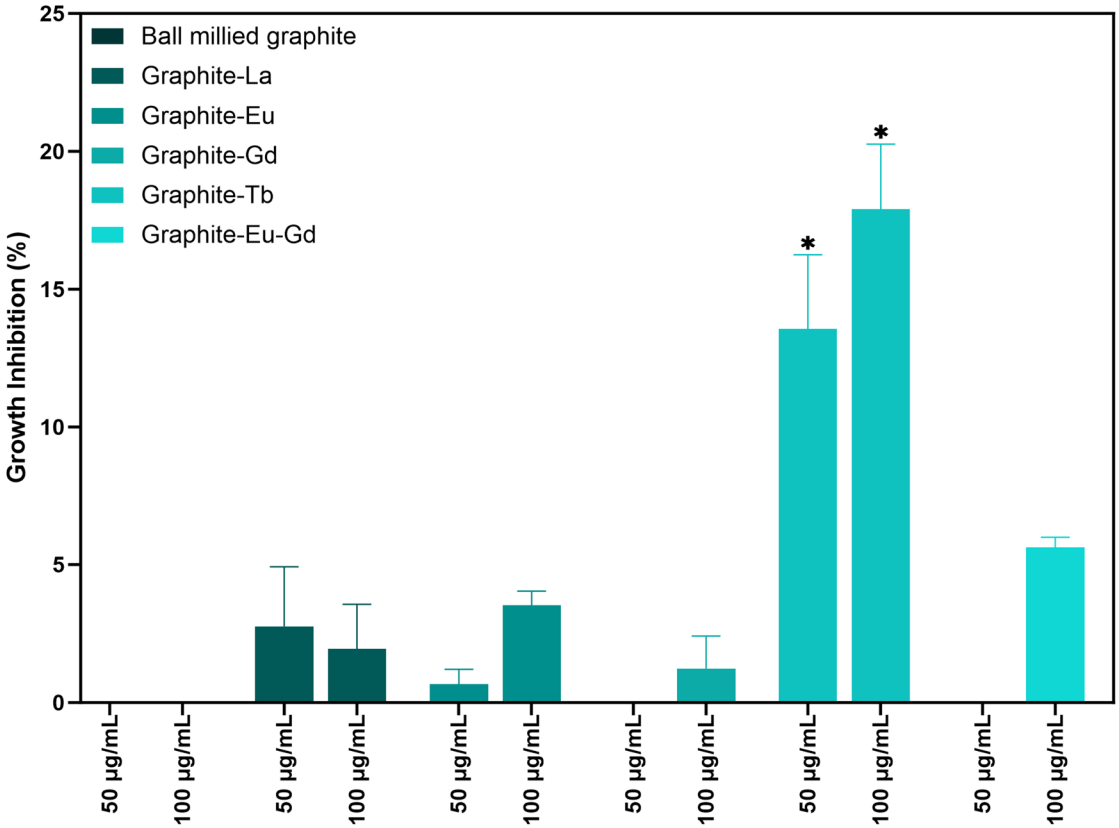

Fig. 11 Growth inhibition (%) of ball milled graphite and graphite-Ln nanocomposites at 50 and 100 µg mL^{-1}. The data were expressed as the standard error of the mean and *$p < 0.05$ (2-way ANOVA).

samples showed a minimal influence of the oxides on the combustion temperature, suggesting a potential role of Gd and Tb oxides in retarding carbon backbone burning.

Understanding the interaction between graphene nanomaterials and cells is crucial for evaluating material safety. The cytotoxicity of GNMs can vary depending on factors such as surface chemistry, size, purity, and dose.[88] Graphene oxide, for example, has been reported to decrease cell viability and induce cell death,[88] with surface charge playing a significant role in the interaction with cells. Studies suggest that GO can interact with cell membranes through electrostatic[89] and hydrophobic[90,91] interactions, leading to membrane damage and cytotoxic effects.

Also, the type and concentration of oxygen-containing moieties[92] influence the outcome and the cytotoxicity induced is higher for GO than for reduced graphene oxide. Additionally, small-size GNMs can penetrate cell membranes because of their sharp edges, causing leakage of cytoplasm.[92] They can also induce the generation of reactive oxygen species,[92] which in turn causes lipid peroxidation, leading to cell death. Impurities in GNMs, such as metallic impurities, organic solvents, chemical oxidisers and reducing agents employed in the preparation of GO and rGO, also affect the toxicity.[88] The introduction of lanthanides to GO can alter the surface charge and thus the interaction with cell membranes. La@GO composites have been reported to exhibit strong bactericidal effects,[93] based on phospholipid dephosphorylation, lipid peroxidation of cell membranes, and disruption of cell walls. Hence, we decided to investigate the cytotoxicity of ball milled graphite and graphite-Ln nanocomposites on COS-7 monkey kidney cells by means of an SRB assay, which is widely used as a model in mammal toxicity tests.[94] The results, presented in Fig. 11 and Table 5, show that ball milled graphite exhibited no cytotoxicity at concentrations of 50 and 100 µg mL^{-1}, possibly due to electrostatic repulsion between graphene nanosheets and cell membranes. In contrast, graphite-Ln nanocomposites showed dose-dependent cytotoxicity, with varying degrees of growth

Table 5 Growth inhibition (%) of ball milled graphite and graphite-Ln nanocomposites against COS-7 cell line at 50 and 100 µg mL^{-1} concentration calculated by detection of SRB. NC = non-cytotoxic. The data is expressed as the standard deviation and *$p < 0.05$ (2way ANOVA)

	Concentration	
Sample	50 µg mL^{-1} [%]	100 µg mL^{-1} [%]
Ball milled graphite	NC	NC
Graphite-La	2.7 ± 2.1	1.9 ± 1.6
Graphite-Eu	0.6 ± 0.5	3.5 ± 0.5
Graphite-Gd	NC	1.2 ± 1.1
Graphite-Tb	13.5 ± 2.7	17.9 ± 2.3
Graphite-Eu-Gd	NC	5.6 ± 0.3

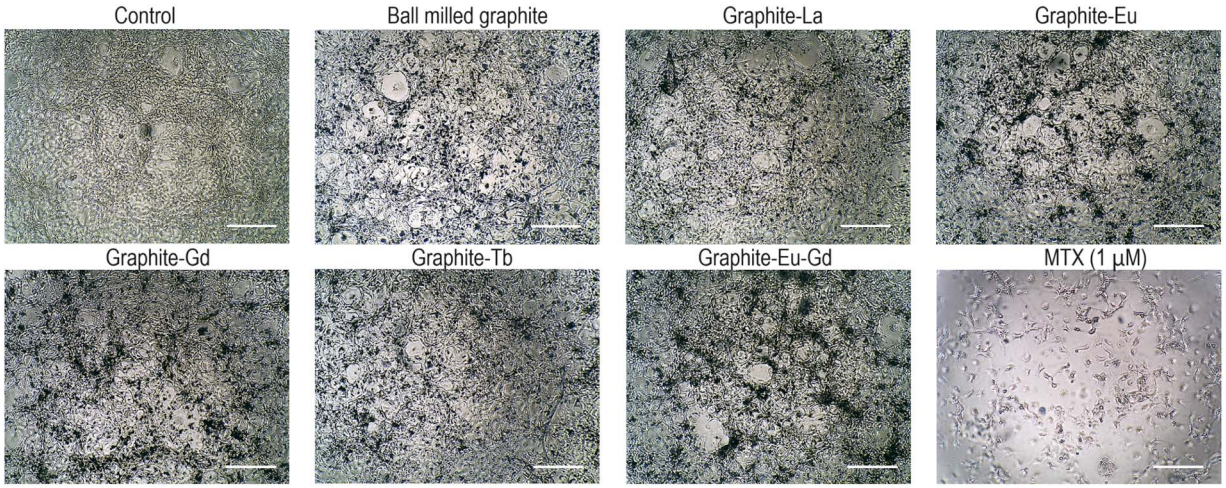

Fig. 12 Cell culture micrographs of the COS-7 line treated with fresh supplemented media as control, ball milled graphite and graphite-Ln nanocomposites at 100 μg mL^{-1}. Scale bar 250 μm.

inhibition. For a concentration of 50 μg mL^{-1}, the cytotoxicity is less than 3% for graphite-La (2.7%) and even less for graphite-Eu (0.6%), graphite-Gd (NC) and graphite-Eu-Gd (NC) but for graphite-Tb, it was considerably higher (13.5%). For a concentration of 100 μg mL^{-1}, the cytotoxicity was again higher for graphite-Tb (17.9%) than for graphite-Eu-Gd (5.6%), graphite-Eu (3.5), graphite-La (2.9%) and graphite-Gd (1.2%). These results correlate with the value of the I_D/I_G ratio obtained from Raman spectroscopy. Thus, it is possible that next to the changes in the surface charge of graphene nanosheets induced by the lanthanide ions, the decrease in size of graphene nanosheets favours cytotoxicity. Morphological analysis of COS-7 monolayer cultures with control and graphite-Ln nanocomposites (Fig. 12) confirmed material aggregation in all cases but revealed no significant changes at the tested concentrations. These findings are comparable to those obtained by González *et al.*[83] and support the hypothesis that lanthanide-modified graphite exhibits altered toxicity behaviour compared to pristine graphite as well as to lanthanide complexes,[95] and underscores the importance of undertaking more thorough studies to fully understand the cytotoxic effects of graphite-Ln nanocomposites and mitigate them for potential applications.

Conclusions

In this study, we have presented a straightforward, cost-effective, and environmentally friendly approach for synthesizing graphite-lanthanide oxide nanocomposites employing ball milling. The mechanochemical functionalisation was accomplished without the need for solvents, hazardous chemicals, and oxidant reagents, requiring only an air atmosphere.

X-ray photoelectron spectroscopy confirmed the successful functionalisation of the graphene nanosheets with hydroxyl, epoxy, and carbonyl groups, providing anchoring sites for lanthanide ions. Raman spectroscopy demonstrated the partial exfoliation of graphite into few-layer graphene in all milled samples, as indicated by the appearance of the D′ band, change in symmetry and a downshift of the 2D band. X-ray diffraction analysis revealed that despite 48 hours of milling, all samples maintained their crystalline structure, supporting that graphite exfoliation took place. Scanning electron microscopy with secondary electron detection showed a reduction in graphite crystallite size, ranging from 1 to 6 μm after milling, consistent with observations from Raman and XRD analyses. The micrographs collected with the backscattered electron detector demonstrated a uniform dispersion of micro- and nanometre-sized lanthanide oxide particles over the graphene nanosheets while scanning transmission electron microscopy with high-angle annular dark-field detection confirmed the presence of lanthanide-containing nanoparticles with lateral dimensions of at least 50–100 nm in all the nanocomposites. The thermogravimetric analysis further supported the presence of oxygen functional groups post-mechanochemical treatment, with weight loss initiating before 550 °C in all nanocomposite thermograms. Interestingly, TGA revealed a catalytic effect of lanthanum and europium oxides, accelerating the graphite combustion, while gadolinium and terbium oxides retarded the combustion process. Moreover, cytotoxicity tests indicated that growth inhibition exerted by graphite-lanthanide oxide nanocomposites did not exceed 5% for concentrations of 50 and 100 μg mL^{-1}, except for the graphite-Tb samples, for which the growth inhibition reached 17.9% at 100 μg mL^{-1}.

In conclusion, our study highlights the feasibility of producing graphite-lanthanide oxide nanocomposites *via* mechanochemical treatment with promising low cytotoxicity profiles and underscores their potential for applications in various fields, from catalysis to biomedicine, emphasising the importance of further investigation of their properties and applications.

Data availability

The data is included in the article and the ESI.†

Author contributions

Diego A. Acevedo-Guzmán: investigation, data curation, formal analysis, validation, visualization, writing – original draft. Brian Monroy-Torres: investigation, validation, visualization. Petra Rudolf: supervision, validation, visualization, writing – review & editing. Vladimir A. Basiuk: investigation, methodology, validation, writing – review & editing. Elena V. Basiuk: conceptualization, methodology, validation, supervision, project administration, funding acquisition, writing – review & editing.

Conflicts of interest

There are no conflicts to declare.

Acknowledgements

Financial support from the National Autonomous University of Mexico (UNAM, grant DGAPA-IN100821) is greatly acknowledged. D. A. A.-G. is indebted to the Postgraduate Program in Chemical Sciences of UNAM, the National Council of Humanities Science and Technology of Mexico (CONAHCyT), and the Double-Degree PhD Program of UNAM with the University of Groningen for a PhD Scholarship. The authors are also grateful to the University Laboratory of Spectroscopic Characterisation of UNAM (LUCE-ICAT-UNAM) for the use of Raman equipment.

References

1 W. Ren and H. M. Cheng, *Nat. Nanotechnol.*, 2014, **9**(10), 726–730.
2 M. Lotya, P. J. King, U. Khan, S. De and J. N. Coleman, *ACS Nano*, 2010, **4**, 3155–3162.
3 Y. Hong, Z. Wang and X. Jin, *Sci. Rep.*, 2013, **3**(1), 1–6.
4 J. M. Munuera, J. I. Paredes, M. Enterría, A. Pagán, S. Villar-Rodil, M. F. R. Pereira, J. I. Martins, J. L. Figueiredo, J. L. Cenis, A. Martínez-Alonso and J. M. D. Tascón, *ACS Appl. Mater. Interfaces*, 2017, **9**, 24085–24099.
5 M. Yi, Z. Shen, S. Ma and X. Zhang, *J. Nanopart. Res.*, 2012, **14**, 1–9.
6 M. Buzaglo, M. Shtein, S. Kober, R. Lovrinčić, A. Vilan and O. Regev, *Phys. Chem. Chem. Phys.*, 2013, **15**, 4428–4435.
7 J. H. Ding, H. R. Zhao and H. Bin Yu, *Sci. Rep.*, 2018, **8**(1), 1–8.
8 X. An, T. Simmons, R. Shah, C. Wolfe, K. M. Lewis, M. Washington, S. K. Nayak, S. Talapatra and S. Kar, *Nano Lett.*, 2010, **10**, 4295–4301.
9 H. Yang, Y. Hernandez, A. Schlierf, A. Felten, A. Eckmann, S. Johal, P. Louette, J. J. Pireaux, X. Feng, K. Mullen, V. Palermo and C. Casiraghi, *Carbon*, 2013, **53**, 357–365.
10 M. Lotya, Y. Hernandez, P. J. King, R. J. Smith, V. Nicolosi, L. S. Karlsson, F. M. Blighe, S. De, W. Zhiming, I. T. McGovern, G. S. Duesberg and J. N. Coleman, *J. Am. Chem. Soc.*, 2009, **131**, 3611–3620.
11 H. Gao, K. Zhu, G. Hu and C. Xue, *Chem. Eng. J.*, 2017, **308**, 872–879.
12 A. M. Dimiev and S. Eigler, *Graphene Oxide: Fundamentals and Applications*, Wiley, 2016.
13 K. Krishnamoorthy, M. Veerapandian, K. Yun and S. J. Kim, *Carbon*, 2013, **53**, 38–49.
14 L. Luo, T. Peng, M. Yuan, H. Sun, S. Dai and L. Wang, *Sensors*, 2018, **18**, 3745.
15 B. C. Brodie, *Philos. Trans. R. Soc. London*, 1859, **149**, 249–259.
16 L. Staudenmaier, *Ber. Dtsch. Chem. Ges.*, 1898, **31**, 1481–1487.
17 U. Hofmann and E. König, *Z. Anorg. Allg. Chem.*, 1937, **234**, 311–336.
18 W. S. Hummers and R. E. Offeman, *J. Am. Chem. Soc.*, 1958, **80**, 1339.
19 C. Jiang, D. An, Z. Wang, S. Zhang, X. An, J. Bo, G. Yan, K. S. Moon and C. Wong, *J. Cleaner Prod.*, 2020, **268**, 122019.
20 J. Andersen and J. Mack, *Green Chem.*, 2018, **20**, 1435–1443.
21 M. N. Temnikov, A. A. Anisimov, P. V. Zhemchugov, D. N. Kholodkov, A. S. Goloveshkin, A. V. Naumkin, S. M. Chistovalov, D. Katsoulis and A. M. Muzafarov, *Green Chem.*, 2018, **20**, 1962–1969.
22 S. Menuel, B. Léger, A. Addad, E. Monflier and F. Hapiot, *Green Chem.*, 2016, **18**, 5500–5509.
23 R. K. Bhuyan, R. K. Mohapatra, G. Nath, B. K. Sahoo, D. Das and D. Pamu, *J. Mater. Sci.: Mater. Electron.*, 2020, **31**, 628–636.
24 X. Li, J. Shen, C. Wu and K. Wu, *Small*, 2019, **15**, 1805567.
25 J. Xu, J. Shui, J. Wang, M. Wang, H. K. Liu, S. X. Dou, I. Y. Jeon, J. M. Seo, J. B. Baek and L. Dai, *ACS Nano*, 2014, **8**, 10920–10930.
26 N. Rubio, C. Fabbro, M. A. Herrero, A. De La Hoz, M. Meneghetti, J. L. G. Fierro, M. Prato and E. Vázquez, *Small*, 2011, **7**, 665–674.
27 R. B. N. Baig and R. S. Varma, *Chem. Soc. Rev.*, 2012, **41**, 1559–1584.
28 R. S. Varma, *Green Chem.*, 2008, **10**, 1129–1130.
29 M. Yi and Z. Shen, *J. Mater. Chem. A*, 2015, **3**, 11700–11715.
30 E. Colacino, G. Ennas, I. Halász, A. Porcheddu and A. Scano, *Mechanochemistry: a practical introduction from soft to hard materials*, 2020.
31 L. Liu, Z. Xiong, D. Hu, G. Wu and P. Chen, *Chem. Commun.*, 2013, **49**, 7890–7892.
32 V. León, M. Quintana, M. A. Herrero, J. L. G. Fierro, A. D. La Hoz, M. Prato and E. Vázquez, *Chem. Commun.*, 2011, **47**, 10936–10938.
33 A. E. D. Mahmoud, A. Stolle and M. Stelter, *ACS Sustain. Chem. Eng.*, 2018, **6**, 6358–6369.
34 O. Yu. Posudievsky, O. A. Khazieieva, V. G. Koshechko and V. D. Pokhodenko, *J. Mater. Chem.*, 2012, **22**, 12465.
35 G. Bharath, R. Madhu, S. M. Chen, V. Veeramani, D. Mangalaraj and N. Ponpandian, *J. Mater. Chem. A*, 2015, **3**, 15529–15539.
36 O. Y. Posudievsky, O. A. Kozarenko, O. A. Khazieieva, V. G. Koshechko and V. D. Pokhodenko, *J. Mater. Chem. A*, 2013, **1**, 6658–6663.
37 J. Chen, W. Chen, D. Song, B. Lai, Y. Sheng and L. Yan, *New J. Chem.*, 2019, **43**, 7057–7064.
38 W. Zhao, M. Fang, F. Wu, H. Wu, L. Wang and G. Chen, *J. Mater. Chem.*, 2010, **20**, 5817–5819.

39 J. Zhang, Z. Zhang, Y. Jiao, H. Yang, Y. Li, J. Zhang and P. Gao, *J. Power Sources*, 2019, **419**, 99–105.
40 M. Chen, C. Huo, Y. Li and J. Wang, *ACS Sustain. Chem. Eng.*, 2016, **4**, 1296–1302.
41 R. Rajagopal and K. S. Ryu, *J. Ind. Eng. Chem.*, 2018, **60**, 441–450.
42 S. Karthikeyan, M. Selvapandiyan and A. Sankar, *Inorg. Chem. Commun.*, 2022, **139**, 109331.
43 P. Aryanrad, H. R. Naderi, E. Kohan, M. R. Ganjali, M. Baghernejad and A. Shiralizadeh Dezfuli, *RSC Adv.*, 2020, **10**, 17543–17551.
44 H. R. Naderi, M. R. Ganjali and A. S. Dezfuli, *J. Mater. Sci.: Mater. Electron.*, 2018, **29**, 3035–3044.
45 L. P. Lingamdinne, S. Lee, J. S. Choi, V. R. Lebaka, V. R. P. Durbaka and J. R. Koduru, *J. Hazard. Mater.*, 2021, **402**, 123882.
46 H. Gao, Y. Zhou, K. Chen and X. Li, *Mater. Res. Bull.*, 2016, **77**, 111–114.
47 X. Song, S. Li, H. Guo, W. You, X. Shang, R. Li, D. Tu, W. Zheng, Z. Chen, H. Yang and X. Chen, *Angew. Chem., Int. Ed.*, 2019, **58**, 18981–18986.
48 Y. Wang, Y. Li, W. Qi and Y. Song, *Chem. Commun.*, 2015, **51**, 11022–11025.
49 S. S. Shinde, A. Sami and J. H. Lee, *Electrochim. Acta*, 2016, **214**, 173–181.
50 V. A. Basiuk, D. A. Acevedo-Guzmán, V. Meza-Laguna, E. Álvarez-Zauco, L. Huerta, M. Serrano, M. Kakazey and E. V. Basiuk, *Mater. Today Commun.*, 2021, **26**, 102030.
51 O. Ivashenko, H. Logtenberg, J. Areephong, A. C. Coleman, P. V. Wesenhagen, E. M. Geertsema, N. Heureux, B. L. Feringa, P. Rudolf and W. R. Browne, *J. Phys. Chem. C*, 2011, **115**, 22965–22975.
52 J. F. Moulder, W. F. Stickle, P. E. Sobol and K. D. Bomben, *Google Scholar*, 2002, **128**.
53 P. Dash, T. Dash, T. K. Rout, A. K. Sahu, S. K. Biswal and B. K. Mishra, *RSC Adv.*, 2016, **6**, 12657–12668.
54 H. Estrade-Szwarckopf, *Carbon*, 2003, **42**, 1713–1721.
55 L. G. Guex, B. Sacchi, K. F. Peuvot, R. L. Andersson, A. M. Pourrahimi, V. Ström, S. Farris and R. T. Olsson, *Nanoscale*, 2017, **9**, 9562–9571.
56 G. Eda and M. Chhowalla, *Adv. Mater.*, 2010, **22**, 2392–2415.
57 D. R. Dreyer, A. D. Todd and C. W. Bielawski, *Chem. Soc. Rev.*, 2014, **43**, 5288–5301.
58 R. Yuge, M. Zhang, M. Tomonari, T. Yoshitake, S. Iijima and M. Yudasaka, *ACS Nano*, 2008, **2**, 1865–1870.
59 A. Ganguly, S. Sharma, P. Papakonstantinou and J. Hamilton, *J. Phys. Chem. C*, 2011, **115**, 17009–17019.
60 I. Y. Jeon, Y. R. Shin, G. J. Sohn, H. J. Choi, S. Y. Bae, J. Mahmood, S. M. Jung, J. M. Seo, M. J. Kim, D. W. Chang, L. Dai and J. B. Baek, *Proc. Natl. Acad. Sci. U. S. A.*, 2012, **109**, 5588–5593.
61 I. Y. Jeon, S. Y. Bae, J. M. Seo and J. B. Baek, *Adv. Funct. Mater.*, 2015, **25**, 6961–6975.
62 H. Zhu, Y. Cao, J. Zhang, W. Zhang, Y. Xu, J. Guo, W. Yang and J. Liu, *J. Mater. Sci.*, 2016, **51**, 3675–3683.
63 C. Liu, X. Liu, J. Tan, Q. Wang, H. Wen and C. Zhang, *J. Power Sources*, 2017, **342**, 157–164.
64 Y. Wang, H. Meng, Y. Lu and C. Li, *Chem. Eng. J.*, 2021, **415**, 129009.
65 S. Motozuka, M. Tagaya, N. Ogawa, K. Fukui, M. Nishikawa, K. Shiba, T. Uehara and T. Kobayashi, *Solid State Commun.*, 2014, **190**, 28–32.
66 G. Zhang, S. Sun, D. Yang, J. P. Dodelet and E. Sacher, *Carbon*, 2008, **46**, 196–205.
67 J. Cao, D. Zhang, X. Zhang, S. Wang, J. Han, Y. Zhao, Y. Huang and J. Qin, *Appl. Surf. Sci.*, 2020, **534**, 147630.
68 M. Kralj, A. Supina, D. Čapeta, I. Sović and I. Halasz, *Materialia*, 2020, **14**, 100908.
69 A. A. Green and M. C. Hersam, *Nano Lett.*, 2009, **9**, 4031–4036.
70 D. Graf, F. Molitor, K. Ensslin, C. Stampfer, A. Jungen, C. Hierold and L. Wirtz, *Nano Lett.*, 2007, **7**, 238–242.
71 A. C. Ferrari, J. C. Meyer, V. Scardaci, C. Casiraghi, M. Lazzeri, F. Mauri, S. Piscanec, D. Jiang, K. S. Novoselov, S. Roth and A. K. Geim, *Phys. Rev. Lett.*, 2006, **97**, 187401.
72 D. S. Lee, C. Riedl, B. Krauss, K. Von Klitzing, U. Starke and J. H. Smet, *Nano Lett.*, 2008, **8**, 4320–4325.
73 Z. Ni, Y. Wang, T. Yu and Z. Shen, *Nano Res.*, 2008, **1**, 273–291.
74 L. M. Malard, M. A. Pimenta, G. Dresselhaus and M. S. Dresselhaus, *Phys. Rep.*, 2009, **473**, 51–87.
75 H. Murphy, P. Papakonstantinou and T. I. T. Okpalugo, *J. Vac. Sci. Technol., B: Microelectron. Nanometer Struct.–Process., Meas., Phenom.*, 2006, **24**, 715–720.
76 J. M. Mendoza-Duarte, F. C. Robles-Hernández, C. D. Gomez-Esparza, J. G. Miranda-Hernández, C. G. Garay-Reyes, I. Estrada-Guel and R. Martínez-Sánchez, *J. Environ. Chem. Eng.*, 2020, **8**, 104370.
77 S. Sharma, D. Susan, N. C. Kothiyal and R. Kaur, *Constr. Build. Mater.*, 2018, **177**, 10–22.
78 L. Liu, N. Solin and O. Inganäs, *RSC Adv.*, 2019, **9**, 39758–39767.
79 K. Zhang, Y. Zhang and S. Wang, *Sci. Rep.*, 2013, **3**(1), 1–7.
80 X. Wang, P. F. Fulvio, G. A. Baker, G. M. Veith, R. R. Unocic, S. M. Mahurin, M. Chi and S. Dai, *Chem. Commun.*, 2010, **46**, 4487–4489.
81 V. A. Basiuk, C. U. Mendoza-Domínguez, V. Meza-Laguna, P. Molina-Sevilla, E. Álvarez-Zauco, M. Serrano, M. Vlasova and E. V. Basiuk, *Fullerenes, Nanotubes Carbon Nanostruct.*, 2023, **31**, 815–827.
82 R. V. Salvatierra, S. H. Domingues, M. M. Oliveira and A. J. G. Zarbin, *Carbon*, 2013, **57**, 410–415.
83 V. J. González, A. M. Rodríguez, V. León, J. Frontiñán-Rubio, J. L. G. Fierro, M. Durán-Prado, A. B. Muñoz-García, M. Pavone and E. Vázquez, *Green Chem.*, 2018, **20**, 3581–3592.
84 F. Lin, Y. Qiu, X. Zheng, Z. Duanmu, Q. Lu, B. Huang, L. Tang and B. Lu, *Chem. Eng. J.*, 2022, **437**, 135286.
85 A. C. Ferrari, *Solid State Commun.*, 2007, **143**, 47–57.
86 L. G. Cançado, K. Takai, T. Enoki, M. Endo, Y. A. Kim, H. Mizusaki, A. Jorio, L. N. Coelho, R. Magalhães-Paniago and M. A. Pimenta, *Appl. Phys. Lett.*, 2006, **88**, 163106.
87 T. Xing, L. H. Li, L. Hou, X. Hu, S. Zhou, R. Peter, M. Petravic and Y. Chen, *Carbon*, 2013, **57**, 515–519.

88 C. Liao, Y. Li and S. C. Tjong, *Int. J. Mol. Sci.*, 2018, **19**, 3564.
89 S. Li, A. J. Stein, A. Kruger and R. M. Leblanc, *J. Phys. Chem. C*, 2013, **117**, 16150–16158.
90 G. Duan, Y. Zhang, B. Luan, J. K. Weber, R. W. Zhou, Z. Yang, L. Zhao, J. Xu, J. Luo and R. Zhou, *Sci. Rep.*, 2017, **7**(1), 1–12.
91 X. Hu, H. Lei, X. Zhang and Y. Zhang, *Microsc. Res. Tech.*, 2016, **79**, 721–726.
92 R. Li, L. M. Guiney, C. H. Chang, N. D. Mansukhani, Z. Ji, X. Wang, Y. P. Liao, W. Jiang, B. Sun, M. C. Hersam, A. E. Nel and T. Xia, *ACS Nano*, 2018, **12**, 1390–1402.
93 H. Zheng, Z. Ji, K. R. Roy, M. Gao, Y. Pan, X. Cai, L. Wang, W. Li, C. H. Chang, C. Kaweeteerawat, C. Chen, T. Xia, Y. Zhao and R. Li, *ACS Nano*, 2019, **13**, 11488–11499.
94 D. Ail, D. Nava, I. P. Hwang, E. Brazhnikova, C. Nouvel-Jaillard, A. Dentel, C. Joffrois, L. Rousseau, J. Dégardin, S. Bertin, J. A. Sahel, O. Goureau, S. Picaud and D. Dalkara, *Sci. Adv.*, 2023, **9**, eadg8163.
95 A. Aragon-Muriel, Y. Liscano-Martínez, E. Rufino-Felipe, D. Morales-Morales, J. O. Nate-Garz and D. Polo-Ceron, *Heliyon*, 2017, e04126.